PCCP

PAPER

View Article Online
View Journal | View Issue

Cite this: *Phys. Chem. Chem. Phys.*, 2015, **17**, 19238

Ultrafast photoinduced dynamics of the organolead trihalide perovskite $CH_3NH_3PbI_3$ on mesoporous TiO_2 scaffolds in the 320–920 nm range†

Oliver Flender,‡ Johannes R. Klein,‡ Thomas Lenzer* and Kawon Oum*

Received 4th April 2015,
Accepted 22nd June 2015

DOI: 10.1039/c5cp01973g

www.rsc.org/pccp

We present femtosecond broadband transient absorption experiments for the investigation of the carrier dynamics in the organolead trihalide perovskite $CH_3NH_3PbI_3$. The perovskite was prepared on a mesoporous TiO_2 scaffold either by 1-step deposition from solution or by 2-step methods employing deposition of lead iodide followed by an on-surface reaction with methylammonium iodide. The thin films were characterized by XRD and FTIR chemical mapping. After pumping with an ultrashort laser pulse at 400 or 500 nm, the dynamics were monitored by a broadband supercontinuum reaching from the near IR (920 nm) into the UV. Specifically, the usage of quartz substrates and thin perovskite/TiO_2 films enabled us to cover the spectral development down to 320 nm. The charge carrier dynamics were largely independent from the specific route of perovskite preparation: initial ultrafast carrier relaxation steps with time constants τ_{CC} and τ_{COP} of <0.08, 0.2 and 2.6 ps were assigned to carrier–carrier and carrier–optical phonon scattering. Pronounced sub-band-gap absorption was found in the near IR at early times. Transient carrier temperatures were extracted from a Boltzmann fit to the blue wing of the photobleach band in the time range 0.2–700 ps, allowing us to distinguish between the decay of acoustic phonons (τ_{AP} = 50 and >1000 ps) and Auger recombination (τ_{AR} = 9, 75 and 450 ps). Carrier relaxation was accompanied by formation of an absorption band around 550 nm, with a characteristic structure assignable to a transient Stark effect, *i.e.* a red-shift of the perovskite spectrum due to the appearance of a directed electric field in the material and possibly additional influence of lattice heating. We observed a substantial Stokes shift between the relaxed photobleach and photoluminescence bands. Contributions of unreacted PbI_2 to the transient absorption features appear to be negligible.

1. Introduction

Organolead trihalide perovskites, such as $CH_3NH_3PbI_3$, have emerged as a highly promising class of solar cell materials currently reaching power conversion efficiencies of *ca.* 20%.[1–5] Implementations include (a) perovskite-sensitized solar cells (PSCs), where the perovskite absorber formally substitutes the organic dye of a classical dye-sensitized solar cell,[6,7] (b) meso-superstructured solar cells (MSCs), where the TiO_2 is replaced by insulating Al_2O_3 and the latter merely acts as a mesoporous scaffold,[7,8] and (c) planar heterojunction perovskite solar cells, where a vapor- or solution-deposited perovskite layer takes over light absorption, charge separation as well as electron and hole transport.[1,6,9,10] To fully understand the exceptional light-harvesting properties of such perovskite arrangements, a thorough investigation of their charge carrier dynamics after photoexcitation is required. Particularly powerful in this respect are time-resolved photoluminescence and ultrafast transient absorption techniques.[6,11–16]

Here, we present an investigation of the prototypical hybrid organic–inorganic perovskite $CH_3NH_3PbI_3$ on a mesoporous TiO_2 layer. We put a particular emphasis on the following aspects: (a) different preparation procedures of the perovskite and their implication for its ultrafast carrier dynamics, (b) the spectral dynamics below and above the band edge at 1.6 eV, where we find a pronounced Stokes shift as well as distinct transient sub-band-gap absorption and photobleach features, and (c) the transient optical response of the perovskite down to the deeper UV region which enables us to extract time constants for carrier scattering processes and time-dependent carrier temperatures. It also unveils a red-shift of the complete perovskite absorption spectrum after photoexcitation. The perovskite studies are complemented by transient absorption experiments for lead iodide on mesoporous TiO_2 to investigate a possible influence

Universität Siegen, Physikalische Chemie 2, Adolf-Reichwein-Str. 2, 57076 Siegen, Germany. E-mail: lenzer@chemie.uni-siegen.de, oum@chemie.uni-siegen.de; Fax: +49 271 740 2943; Tel: +49 271 740 2803

† Electronic supplementary information (ESI) available. See DOI: 10.1039/c5cp01973g

‡ These authors contributed equally to this work.

of unreacted PbI_2 on the dynamics. In all cases, monitoring of the optical response from below up to far above the band-gap is made possible by employing multifilament super-continuum probing covering the particularly wide spectral range 320–920 nm.

2. Experimental

Perovskite/TiO_2 and PbI_2/TiO_2 thin films with a thickness of *ca.* 200–300 nm were prepared on glass and quartz substrates. Three different methods of preparation were employed for the perovskite $CH_3NH_3PbI_3$, by adapting different synthesis routes from literature:[17–20] (A) 1-step deposition of a "perovskite solution", (B) 2-step deposition employing consecutive spin- and dip-coating steps of PbI_2 and methylammonium iodide (MAI) solutions (DSSD = double-step spin-dip), and (C) 2-step deposition involving two spin-coating steps of PbI_2 and MAI solutions (DSDS = double-step double-spin). The perovskite samples were characterized by X-ray diffraction (XRD), specular reflectance FTIR spectroscopy/mapping, optical microscopy in the visible range, steady-state UV-Vis-NIR spectroscopy and steady-state photoluminescence spectroscopy. The time-resolved transient absorption spectra of the perovskite and PbI_2 samples in the UV-Vis-NIR range after excitation at 400, 495 and 500 nm were recorded using the pump–supercontinuum probe (PSCP) method.[21–27] Full details are provided in the ESI.†

3. Results and discussion

3.1 XRD patterns and FTIR spectra of $CH_3NH_3PbI_3$

Perovskite samples prepared by the 1-step, 2-step (DSSD) and 2-step (DSDS) methods were investigated by X-ray diffraction and the corresponding patterns are shown in the ESI† (Fig. S1). All characteristic peaks of the perovskite were clearly observed, confirming that tetragonal $CH_3NH_3PbI_3$ had formed.[17,18,20,28] For the 1-step sample, additional peaks from PbI_2 at *ca.* 12.7° and 39.6° were found, possibly due to incomplete reaction. Although an equimolar ratio of precursors was used, the filtering step prior to spin-coating might be the reason for this. As will be shown below, there is however no visible influence of PbI_2 in the optical measurements, neither in the steady-state nor in the transient absorption experiments.

In Fig. 1, we present *in situ* specular reflectance FTIR spectra of MAI (A) and $CH_3NH_3PbI_3$ (B) deposited on a TiO_2/glass substrate. We focus on fingerprint bands of the methylammonium cation above 1250 cm^{-1}, starting with the MAI reference sample in (A). The spectrum is in very good agreement with IR spectra reported by Cabana *et al.* for an α′-phase thin film of MAI.[29] Sharp peaks are located at 1491 cm^{-1} (symmetric NH_3^+ bending) and 1406 cm^{-1} (symmetric CH_3 bending). The peak at 1561 cm^{-1} is due to asymmetric NH_3^+ bending. The broad band with a maximum at 3092 cm^{-1} and an additional peak at 2962 cm^{-1} is due to NH_3^+ and CH_3 stretching vibrations and further broadened likely because of hydrogen-bonding, crystal splittings and Fermi-resonance.[29] The shoulder-like feature

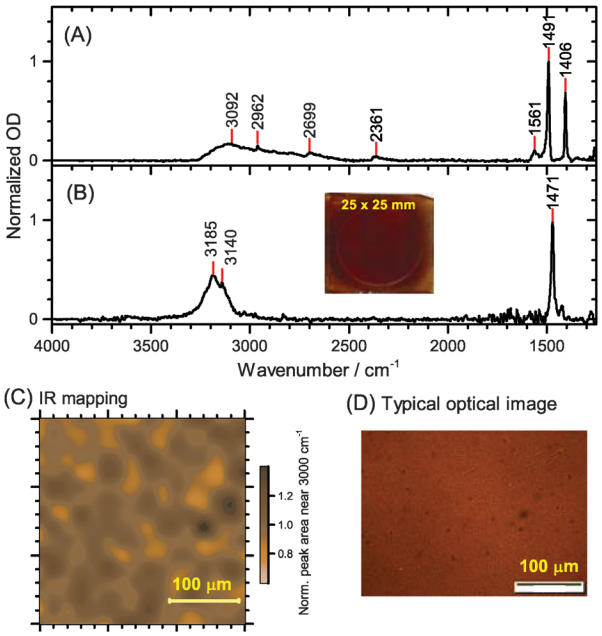

Fig. 1 FTIR absorption spectra recorded in specular reflectance mode for (A) methylammonium iodide and (B) $CH_3NH_3PbI_3$, both deposited on TiO_2/glass. Spectra are obtained from a *ca.* 20 µm diameter spot and are normalized to the highest peak. The wavenumber of each peak is given on top of each spectrum. The photograph in (B) shows the complete perovskite sample on a 25 × 25 mm^2 substrate (DSDS method). In (C), the result of FTIR mapping of the 2900–3400 cm^{-1} band from (B) is shown for a 300 × 300 μm^2 thin film area. Individual OD values were scaled, so that the mean OD value over the whole area is unity. The picture of the thin film in (D) was taken with an optical microscope (whitelight illumination, transmission mode).

which tails off toward 2200 cm^{-1}, is mainly composed of combination bands, for a detailed assignment see ref. 29.

For the perovskite sample (B) (see also the photograph), the symmetric NH_3^+ bending mode of $CH_3NH_3^+$ is slightly red-shifted (1471 cm^{-1}) and broadened. According to Onoda-Yamamuro *et al.*, broadening could be due to rapid reorientation of the cation around its CN axis.[30] The peak assigned to the asymmetric NH_3^+ bending mode has practically disappeared, and the peak observed at 1406 cm^{-1} is just visible as a weak shoulder. The width of the NH_3^+ and CH_3 stretching region (2900–3200 cm^{-1}) is narrower, and the long "tail" of combination bands observed for the MAI thin film is not seen. We note that our spectrum differs from the previously published FTIR spectrum of $CH_3NH_3PbI_3$ in a KBr pellet obtained by Jeon *et al.*,[31] in the region above 3300 cm^{-1}. We do not see a distinct additional band at 3450 cm^{-1}, in agreement with our spectrum of MAI.

As expected, no IR absorption peaks were observed for a PbI_2 reference sample spin-coated on TiO_2/glass in the wavenumber range above 1250 cm^{-1} investigated here, because phonon modes for this heavy-atom system are all located below 150 cm^{-1}.[32–34]

We also performed chemical mapping of the perovskite thin film structure by FTIR spectroscopy using the integral of the 2900–3400 cm^{-1} fingerprint band in Fig. 1(B) to obtain an overview of the thin film morphology. We used a 16 × 16 grid with 20 µm step size where each mapping point sampled a diameter of roughly 20 µm. Results are shown in Fig. 1(C)

(an optical microscope picture is shown in (D), see ESI† for more pictures). The standard deviation of the IR optical density (OD) in this area is about 12%. We see connected islands of higher OD regions which correlate with structures seen on previous SEM images of such perovskite thin films.[28] In the time-resolved experiments reported below, we employ a 120 μm diameter probe beam and also move the sample constantly within a typical area of 2 × 2 mm^2. The results of the time-resolved experiments will therefore represent perovskite dynamics averaged over these different domains.

3.2 Steady-state absorption and photoluminescence

Steady-state absorption spectra of $CH_3NH_3PbI_3$ are presented in Fig. 2. The black solid line corresponds to the spectrum of perovskite prepared by the 1-step method on TiO_2/glass. The red and green solid lines represent the spectra on TiO_2/glass and TiO_2/quartz, respectively, obtained using 2-step preparation (DSDS and DSSD). Most importantly, the shape of the absorption spectra largely agrees. The remaining differences are due to the different scattering properties of each sample combined with the normalization procedure used in Fig. 2. Thus the specific preparation routes employed in the current experiments apparently have only a small influence on the resulting absorption properties of the material.

The spectra show a rather flat increase toward the UV, containing two characteristic features, a step at *ca.* 13 100 cm^{-1} (1.6 eV, 763 nm) and a shoulder at *ca.* 21 000 cm^{-1} (2.6 eV, 480 nm). The general shape of the absorption spectrum was successfully reproduced by calculations for the tetragonal perovskite structure of De Angelis and co-workers,[35,36] with the low-energy step corresponding to the direct transition between the valence band (VB) and the conduction band (CB) at the Γ point of the Brillouin zone of $CH_3NH_3PbI_3$.

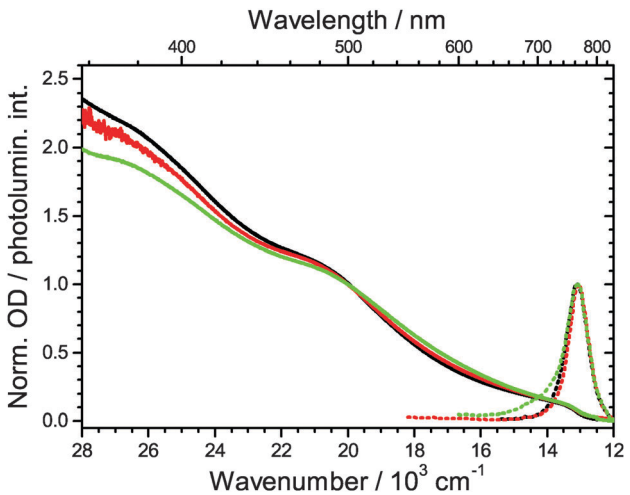

Fig. 2 Steady-state absorption (solid lines) and photoluminescence spectra (dotted lines) of the perovskite $CH_3NH_3PbI_3$ on a *ca.* 300 nm thick TiO_2 nanoparticle film attached to different substrates. Black: 1-step deposition of the perovskite on TiO_2/glass. Red and green: 2-step deposition procedure on TiO_2/glass (DSDS) and TiO_2/quartz (DSSD), respectively. For an easier comparison, absorption spectra are set to Zero at 12 000 cm^{-1} and normalized at 20 000 cm^{-1}. Photoluminescence spectra are normalized at their maxima.

The photoluminescence spectra, shown in Fig. 2 as black, red and green dotted lines, consist of a single, sharp emission band, approximately centered at the step of the band-gap absorption, for TiO_2/glass (1-step) at 13 090 cm^{-1} (764 nm) with an FWHM of 770 cm^{-1}, for TiO_2/glass (2-step, DSDS) at 13 050 cm^{-1} (766 nm) with an FWHM of 700 cm^{-1}, and for TiO_2/quartz (2-step, DSSD) at 13 090 cm^{-1} (764 nm) with an FWHM of 820 cm^{-1}. The feature arises from radiative electron–hole recombination at the edge of the VB and CB. The FWHM values are in excellent agreement with a simple estimate of 700 cm^{-1} at 296 K obtained from a line shape analysis according to ref. 37.

3.3 Ultrafast perovskite dynamics after excitation at 500 nm

In Fig. 3, we present broadband transient absorption spectra (365–770 nm) of perovskite/TiO_2/glass prepared by the 1-step method. The pump wavelength of 500 nm produces charge

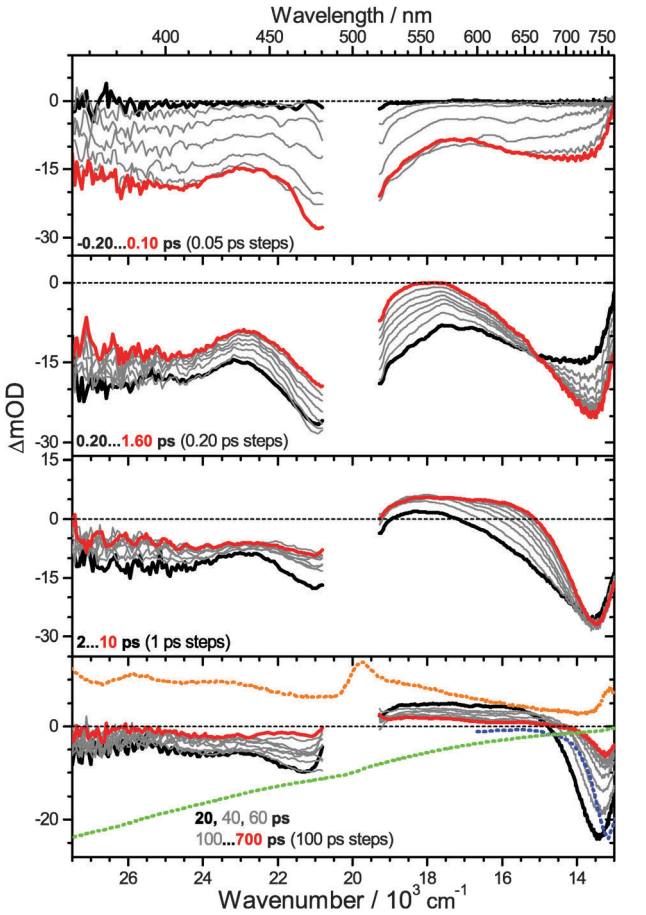

Fig. 3 Transient PSCP absorption spectra of $CH_3NH_3PbI_3$ (1-step deposition on TiO_2/glass) after excitation at 500 nm: (first panel) −0.20…0.10 ps with 50 fs steps; (second panel) 0.20…1.60 ps with 0.20 ps steps; (third panel) 2…10 ps with 1 ps steps; (fourth panel) 20, 40, 60 ps and 100…700 ps (100 ps steps). Selected transient spectra are shown as thick colored lines for guidance. The green dotted line in the bottom panel corresponds to the inverted and scaled steady-state absorption spectrum; the orange-dotted line is the smoothed and scaled first derivative of the steady-state absorption spectrum; the blue-dotted line corresponds to the scaled steady-state stimulated emission spectrum of $CH_3NH_3PbI_3$. The OD at the excitation wavelength was 0.57.

carriers with an excess energy of 6900 cm^{-1} above the band gap (corresponding to $E_{initial} = 1.53 \cdot E_{bg}$). Data in an interval of ±20 nm around the center pump wavelength are not shown because of substantial pump-light scattering of the sample. The lower probe wavelength limit of ~365 nm is set by strong absorption of the perovskite/TiO_2 thin film.

The spectral development around $t = 0$ is shown in the top panel. A negative signal appears over the entire wavelength range. It arises from instantaneous photobleaching because electrons are excited from the valence band to the conduction band. In addition, one expects ultrafast carrier–carrier scattering which results in very fast initial spreading of holes and electrons along the energy axis and thus an additional broadening of the bleach.[22,38] There is a broad negative band appearing around 480 nm (partly obscured by the scattered pump light), and one notices the earliest portion of the build-up of a pronounced bleach band around 720 nm, *i.e.* near the band edge of the perovskite. The process is assigned to the initial phase of carrier relaxation toward the band edge which is ultrafast (within the time resolution of our setup) due to efficient carrier–carrier and carrier–optical phonon scattering.[22,38]

The second panel shows the dynamics up to 1.6 ps. The bleach feature at 720 nm progressively increases due to band-filling,[39] sharpens and shifts to the red. At the same time, the bleach below 660 nm decays, and one notices the appearance of an absorption feature in the range near 550 nm. We explain this process by carrier cooling due to mainly carrier–phonon scattering and also slower carrier–carrier scattering contributions. The absorption feature suggests the presence of a local Stark field inducing a red-shift of the perovskite absorption spectrum, *i.e.* an extra absorption contribution in the ΔOD signal (see below). The shift is likely present already at earlier times but is overcompensated by the broad initial bleach.

In the third panel, the spectral development up to 10 ps is shown. The blue side of the bleach feature at 740 nm is further narrowing, and the absorption feature becomes more prominent and extends over the range 520–660 nm by 10 ps. These spectral changes are a clear sign of further cooling of the photoexcited carriers.[37] At the same time, the bleach feature below 500 nm decays in a similar fashion.

In the bottom panel, the spectral dynamics are shown on longer timescales up to 700 ps. Notable are the combined decay of the bleach band (peak located at *ca.* 740 nm, black line) to a constant value which cannot be described by a single exponential function. In agreement with previous studies, we ascribe this effect to Auger recombination,[12] which happens because of the relatively high initial carrier density. The decay is accompanied by a red-shift of the peak.

The shape of the spectrum, especially the broad absorption feature, deserves further discussion. It was previously assigned to absorption of a charge transfer state.[16] However, as will be demonstrated by several examples below, this feature likely originates from a red-shift of the whole perovskite absorption band. Such an effect might result *e.g.* from a Stark effect, *i.e.* the buildup of a directed local electric field,[23,40–43] renormalization of electron and hole states by the transient carrier populations or from lattice heating.[22,44] In such cases, the shape of the spectrum should bear some features of the first derivative of the absorption spectrum (orange and green dotted lines in the bottom panel of Fig. 3, respectively). Indeed, the derivative shows positive amplitude over this spectral range, and this interpretation will be backed up by the spectral features in the experiments reported in the sections below.

3.4 Spectral dynamics near the perovskite band edge

In the following, we highlight the ultrafast dynamics close to the perovskite band edge in more detail. We performed PSCP experiments covering the dynamics in the 520–920 nm range, see Fig. 4. The sample was again excited at 500 nm.

The first two panels show the build-up of the extended bleach feature which quickly converts into a pronounced peak. At the same, the peak shifts to the red (compare Section 3.3).

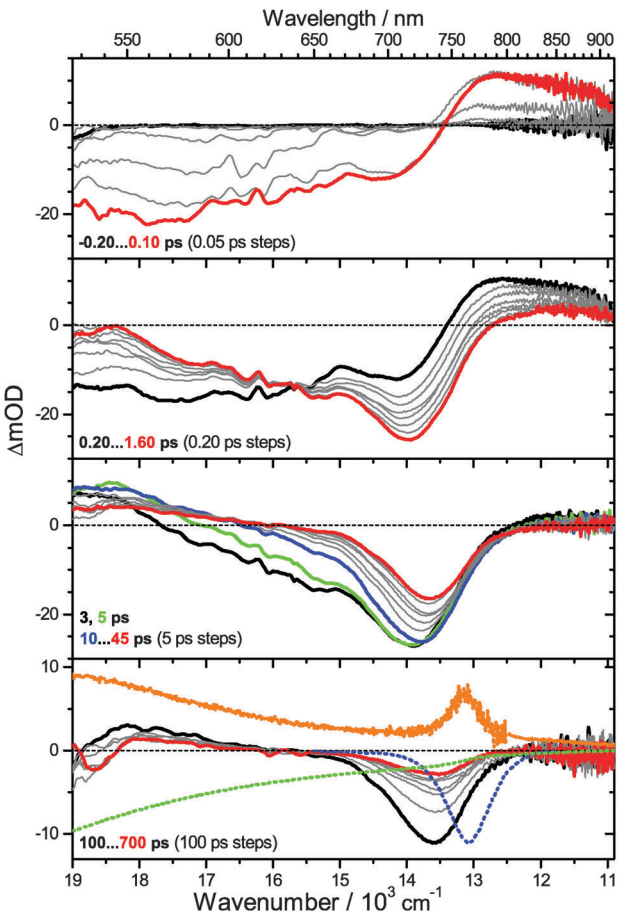

Fig. 4 Transient PSCP absorption spectra showing the dynamics of $CH_3NH_3PbI_3$ on TiO_2/glass (1-step deposition) near the band gap for excitation at 500 nm: (first panel) −0.20…0.10 ps with 50 fs steps; (second panel) 0.20…1.60 ps with 0.20 ps steps; (third panel) 3, 5 and 10…45 ps with 5 ps steps; (fourth panel) 100…700 ps (100 ps steps). Selected transient spectra are shown as thick colored lines for guidance. The dotted lines in the bottom panel correspond to: the inverted and scaled steady-state absorption spectrum (green), the smoothed and scaled derivative of the steady-state absorption spectrum (orange) and the steady-state stimulated emission spectrum (blue) of $CH_3NH_3PbI_3$. The OD at the excitation wavelength was 0.75.

Notably, there is a pronounced sub-band-gap absorption extending at least out to 920 nm. It immediately forms upon photoexcitation. The ultrafast decay of the absorption correlates with the formation of the bleach peak. The sub-band-gap absorption feature of $CH_3NH_3PbI_3$ could result from band gap renormalization due to carrier exchange and correlation effects, similarly to what was previously observed for GaAs:[45] the absorption band edge shifts to the red, once free carriers are generated. The dynamics in the bleach region are due to band-filling by relaxation of charge carriers toward the band edge.

In the third panel, the dynamics up to 45 ps are shown. The bleach feature further sharpens and shifts to the red, highlighting additional carrier cooling due to carrier–phonon and phonon–phonon scattering. The decay of the bleach is due to Auger recombination, as explained above.

In the bottom panel, we present the dynamics up to 700 ps. The bleach feature further shifts to the red and decays. After 700 ps, Auger recombination has ceased and the signal stays at a constant level. Notably, the width of the bleach feature (1270 cm^{-1}, black line at 100 ps) is wider than the width of the steady-state emission (SE) spectrum (760 cm^{-1}, blue dotted line), and its peak is also shifted further to the blue than the SE. We therefore believe that the negative feature in the PSCP spectra represents a superposition of a band-filling contribution at shorter wavelength and the Stokes-shifted stimulated emission feature, the latter being partly canceled by a contribution from the Stark effect. The latter contribution may be again estimated by taking the first derivative (orange-dotted line) of the steady-state absorption spectrum (green dotted line, inverted in Fig. 4). We see that the peak feature of the derivative, is located at the same position as the SE, but has opposite sign. In addition, the Stark effect nicely explains the absorption feature below 600 nm: here, the derivative has positive amplitude, and it even has the same slope as the PSCP spectra in these spectral regions. Therefore, this makes the postulation of an excited complex undergoing charge transfer[16] unnecessary.

3.5 Perovskite dynamics upon 400 nm excitation

To investigate the dependence of the perovskite dynamics on initial excitation energy, we also carried out experiments at the pump wavelength 400 nm (11 900 cm^{-1} above the band gap, corresponding to $E_{initial} = 1.91 \cdot E_{bg}$). In order to monitor the dynamics down to the shortest wavelengths possible, the perovskite layer was prepared on a TiO_2/quartz substrate by the 2-step method (DSSD). This way the lower wavelength limit can be extended down to 320 nm. PSCP spectra are shown in Fig. 5.

The top panel shows the appearance of a broad bleach feature around zero delay time. The same characteristic bleach peak around 490 nm appears, as already seen in Fig. 3 for excitation at 500 nm. However, the bleach band falls off more steeply toward the red than for 500 nm excitation. There is again a clear contribution of ultrafast carrier–carrier scattering (within the time-resolution of the setup) visible by the tail progressively extending toward the red (compare *e.g.* the spectra at 0 and 0.1 ps). Upon excitation at 400 nm, carriers require a longer time to relax toward the band edge because of the additional excess energy.

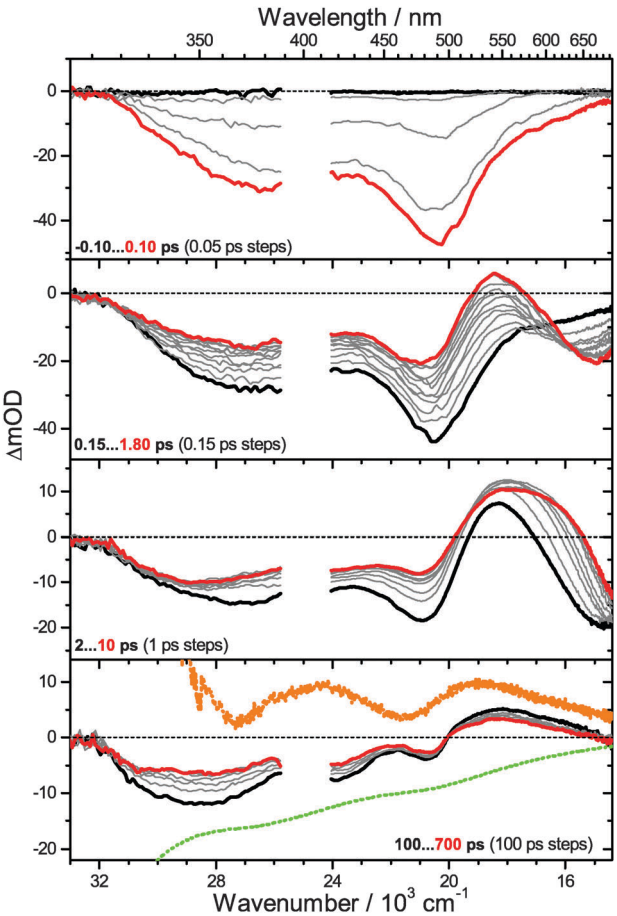

Fig. 5 Transient PSCP absorption spectra of $CH_3NH_3PbI_3$ on TiO_2/quartz (DSSD) for excitation at 400 nm: (first panel) −0.10…0.10 ps with 50 fs steps; (second panel) 0.15…1.80 ps with 0.15 ps steps; (third panel) 2…10 ps with 1 ps steps; (fourth panel) 100…700 ps (100 ps steps). Selected transient spectra are shown as thick colored lines for guidance. In the bottom panel, the green dotted line corresponds to the inverted and scaled steady-state absorption spectrum. The orange-dotted line represents the smoothed and scaled first derivative of the steady-state absorption spectrum. Data in a range of ±800 cm^{-1} around the center pump wavenumber are not shown due to considerable scattered pump light. The OD at the excitation wavelength was 1.19.

Up to 1.8 ps (second panel), further carrier relaxation toward the band edge is observed, resulting in the build-up of the bleach feature above 600 nm. Correspondingly, the bleach amplitude below 600 nm decays and absorption forms around 540 nm. Whereas reduction of the bleach at shorter wavelengths is partially due to the energy loss of the hot carriers due to carrier–carrier and carrier–phonon scattering, additional absorption contributions arise from the Stark effect, as further discussed below.

The carrier relaxation up to 10 ps is depicted in the third panel: the bleach feature shifts even further to the red and leaves the spectral window. The absorption feature rises and extends from 500 to 660 nm by 10 ps. The bleach below 500 nm further decays in a non-uniform fashion suggesting that the region around 500 nm preferentially monitors carrier relaxation toward the band edge. The UV part of the spectrum is less affected,

suggesting that in this region one predominantly monitors Auger recombination of electrons and holes.

The bottom panel shows a uniform decay of the whole spectrum, with an isosbestic point at 500 nm (likely present also in Fig. 3 but in that case obscured by scattered light). Therefore carrier relaxation toward the band edge has been largely achieved, and the uniform decay of the band up to 700 ps is dominated by Auger recombination. Remarkably, the structure over almost the entire spectrum resembles the first derivative (orange dotted-line) of the steady-state absorption spectrum (green-dotted line), clearly pointing to a red-shift of the perovskite absorption spectrum due to the build-up of a substantial electric field across the perovskite layer. Once again, it should be emphasized that similar phenomena have been observed previously for semiconductor quantum dots[40] and at dye-sensitized ZnO and TiO_2 electrodes.[23,41–43,46]

3.6 Kinetic modeling of carrier dynamics for $CH_3NH_3PbI_3$

The carrier dynamics of semiconductors after photoexcitation with a femtosecond laser pulse are known to be exceptionally complex, because a variety of relaxation processes occur on overlapping timescales which comprise a wide range of time constants, from sub-100 fs to the nanosecond range. These include but are not limited to carrier–carrier scattering, carrier–optical phonon scattering, decay of acoustic phonons and carrier recombination.[38] At the same time, presence of a non-equilibrium carrier distribution might induce transient red- or blue-shifts of spectral bands.[47] According to Shah, relaxation can be roughly divided into a coherent regime ($\leq$200 fs), a non-thermal regime ($\leq$2 ps), a hot-excitation regime (*ca.* 1–100 ps) and an isothermal regime ($\geq$200 ps).[38] Here, we attempt to separate specific processes by identifying them on the basis of their characteristic spectral signatures.

(a) Cooling of hot charge carriers. In all PSCP spectra, we observed a characteristic band narrowing and steepening of the band edge between 550 and 750 nm, see *e.g.* Fig. 3 and 5. This high-energy side of the bleach feature corresponds to the exponential tail of the carrier distribution. It is therefore possible to extract time-dependent carrier temperatures using an approach previously applied to transient photoluminescence spectra of semiconductors, such as InGaAs.[37,38] To do so, the high energy tail of the bleach is fitted to an expression proportional to $E^2 \cdot \exp[-E/(k_B \cdot T_{carrier})]$.[37] Fit examples are shown in Fig. S3 (ESI†). A Boltzmann-type tail is visible from 0.2–0.3 ps onwards (see *e.g.* Fig. 3 and Fig. S3, ESI†), suggesting that one enters the thermal regime where assignment of a quasi-temperature appears reasonable. Using this strategy, we are able to separate carrier cooling and carrier recombination processes. Recombination processes mainly reduce band amplitudes (carrier concentrations), whereas the "tail fit" is only sensitive to the slope of the "blue edge" of the band, regardless of the band amplitude.

The resulting time-dependent carrier temperature is plotted in Fig. 6, both on a linear and a logarithmic timescale. Blue circles represent results for excitation at 500 nm (PSCP spectra in Fig. 3). Red circles are for excitation at 400 nm (PSCP spectra in Fig. 5). The data for λ_{pump} = 500 nm show that the carriers

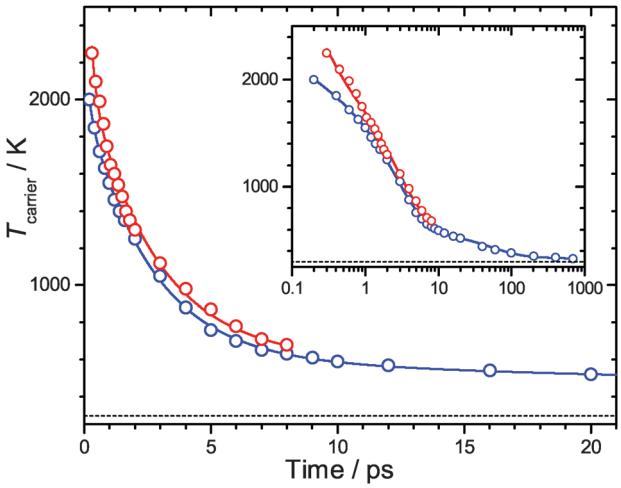

Fig. 6 Time-dependent carrier temperatures extracted from the Boltzmann tail of the carrier distributions seen in the PSCP experiments. (Blue circles) Excitation at 500 nm (PSCP spectra in Fig. 3). (Red circles) Excitation at 400 nm (PSCP spectra in Fig. 5). The inset shows the cooling process on a logarithmic timescale. Solid lines are fit results (see text). The dashed line corresponds to the initial carrier temperature of 296 K (thermal equilibrium).

possess a temperature of about 2000 K at 0.2 ps. We observe a fast decay of the carrier temperature within the first two picoseconds and assign this to carrier–carrier and carrier–optical phonon scattering, in good agreement with what is known for other systems, such as *e.g.* graphene.[22] Afterwards, the temperature decays more slowly, entering the regime where the decay of optical into acoustic phonons becomes important.

By 20 ps, an effective carrier temperature of 520 K is reached. The cooling on longer timescales is governed by slower decay *via* acoustic phonons, corresponding to the extended tail in the logarithmic representation (Fig. 6, inset). This also involves heat conduction to the TiO_2 scaffold and finally (on even longer timescales) to the glass/quartz substrate.[22] A temperature of 330 K is reached at 700 ps.

The experiments for λ_{pump} = 400 nm show consistent behavior: the carrier temperature for λ_{pump} = 400 nm at early times (*e.g.* 1870 K at 1.0 ps) is 21% higher than for λ_{pump} = 500 nm (1550 K at 1.0 ps), in satisfactory agreement with the 25% higher initial energy deposited by photoexcitation. The decay of $T_{carrier}$ shows a similar behavior: only the effective transient temperature is slightly higher, because of the higher initial energy of the carriers. The longer carrier cooling proceeds the closer the two curves approach, as expected from simple theories of carrier cooling in semiconductors.[38]

In Fig. 7 we show representative kinetic traces at the probe wavelengths 470 nm (blue), 575 nm (green) and 760 nm (red). The panels (A) and (A′) on the left side are for excitation at 500 nm, whereas the kinetics for excitation at 400 nm are shown on the right side in panels (B) and (B′). In panel (A′), we observe that the transients at 575 nm and 760 nm show a mirror-image-like rise and decay with the same temporal behavior. A combined fit to the transients at both pump wavelengths provides time constants τ_{CC} and τ_{COP} of 0.2 ps and 2.6 ps for the initial dynamics. These time constants also describe the fast decay of

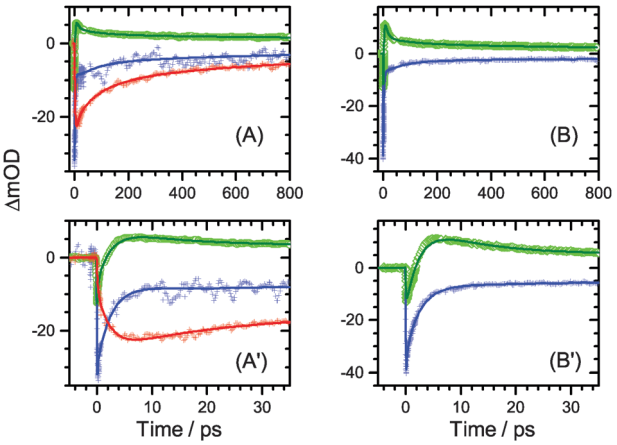

Fig. 7 Kinetic traces from PSCP experiments (symbols) including simulations (lines). (Blue) λ_{probe} = 470 nm, (green) 575 nm, and (red) 760 nm. Results in panels (A) and (A′) are for λ_{pump} = 500 nm (Fig. 3), whereas results in panels (B) and (B′) are for λ_{pump} = 400 nm (Fig. 5). The bottom panels show magnifications of the transients in the corresponding upper panels at early times.

the $T_{carrier}(t)$ curve in Fig. 6 very well. We therefore assign these processes to carrier cooling due to carrier–carrier and carrier–optical phonon scattering. It is noted that the simulations in Fig. 7 require another component of τ_{CC} < 80 fs (time-resolution-limited) which is the ultrafast relaxation process toward the band edge seen in the top panels of Fig. 3 and 5. This must be the fastest part of carrier–carrier scattering in the coherent regime. At this time, it is not yet possible to assign a temperature to the carrier distribution.

The decay of the $T_{carrier}(t)$ curve at longer times is well described by a time constant of τ_{AP} = 50 ps and is assigned to the aforementioned slower cooling process *via* acoustic phonons. In fact, even at the longest times covered by the PSCP experiments, the carrier temperature is still *ca.* 330 K. Cooling down to the equilibrium temperature of 296 K will probably require a few more nanoseconds.

(b) Carrier recombination. Beside changes in its shape due to cooling, the bleach band at 740 nm also exhibits a characteristic decay (see *e.g.* Fig. 3 and 4). As noted above, this is assigned to Auger recombination of electrons and holes. Kinetic analysis provides time constants of 9, 75 and 450 ps for describing this decay (Fig. 7). As expected, this process cannot be described by a single exponential, as it crucially depends on the carrier density. At long times, the transients approach a constant level, suggesting that Auger recombination becomes inefficient.

Time constants from the kinetic analysis are summarized in Table 1. There is considerable overlap of the timescales for relaxation of acoustic phonons and Auger recombination which however can be still disentangled by the analysis provided above. The initial ultrafast dynamics involving carrier–carrier and carrier–optical phonon scattering are well separated from these slower processes.

3.7 Photoinduced dynamics of PbI_2 on TiO_2

It was previously argued that lead iodide, formed by decomposition or thermal treatment,[48–50] may visibly contribute to the dynamics observed in pump–probe transient absorption spectra of $CH_3NH_3PbI_3$.[14] In order to quantify potential contributions to the spectral dynamics observed in our transient spectra for $CH_3NH_3PbI_3$, we performed separate PSCP experiments for neat PbI_2 deposited on TiO_2/glass. Results are shown in Fig. 8 for a pump wavelength of 495 nm which is located on the band edge of the PbI_2 steady-state absorption spectrum (compare the green dotted line in the bottom panel). Therefore, carriers are generated with virtually no excess energy in the

Table 1 Summary of kinetic results for the photoinduced dynamics of $CH_3NH_3PbI_3$ on mesoporous TiO_2 attached to a glass or quartz substrate

τ_{CC}, τ_{COP}[a] (ps)	τ_{AP}[b] (ps)	τ_{AR}[c] (ps)
<0.08, 0.2, 2.6	50, >1000	9, 75, 450

[a] Time constants for carrier–carrier scattering and carrier–optical phonon scattering. [b] Time constants for relaxation *via* acoustic phonons. [c] Time constants for Auger recombination.

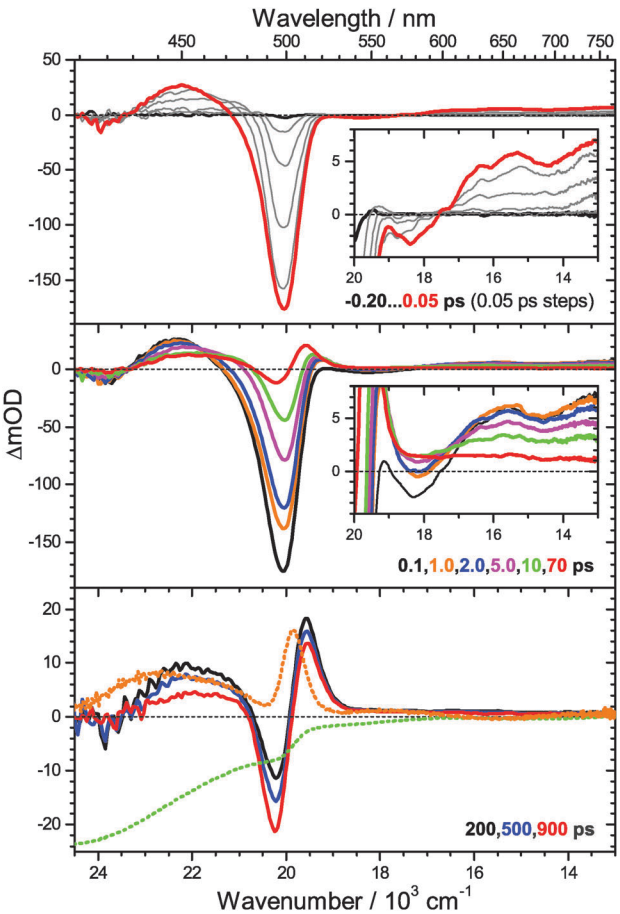

Fig. 8 Transient PSCP absorption spectra of PbI_2 on TiO_2/glass for excitation at 495 nm: (upper panel) −0.20…0.05 ps with 50 fs steps; (middle panel) 0.1, 1.0, 2.0. 5.0, 10, 70 ps; (lower panel) 200, 500, 900 ps. Selected transient spectra are shown as thick colored lines for guidance. In the lower panel, the green dotted line corresponds to the inverted and scaled steady-state absorption spectrum of PbI_2. The orange dotted line represents the smoothed first derivative of the steady-state absorption spectrum. The insets in the top and middle panel show magnifications of the weak "absorption tail" below 20 000 cm^{-1}.

CB and, in contrast to the perovskite dynamics discussed above, there should be no carrier cooling visible.

Around $t = 0$ (top panel), we observe the build-up of a strong negative feature at 500 nm and an absorption band at 450 nm. We assign the bleach feature to band-filling, superimposed by stimulated emission.[51] The absorption feature could possibly arise from a carrier-induced red-shift of the absorption band (compare the first derivative of the steady-state absorption spectrum shown as a dotted orange line in the bottom panel) or from absorption of carriers in the CB, which might be also responsible for the long absorption tail visible in the range 570–770 nm. In addition, very weak oscillatory structure appears instantaneously above 520 nm (see the insets). It arises from the change in refractive index of PbI_2 due to charge carrier generation. A similar oscillatory structure was observed by us previously for dye-sensitized mesoporous ZnO thin films upon ultrafast photoinduced electron injection modifying the refractive index of ZnO.[23] In that case, the modulation width of the oscillations was narrower because of the larger thickness (2 μm) of the thin film. Similar interference structures were also found previously for neat ZnO surfaces when electrons were generated in the CB either optically or electrochemically.[52,53] The visibility of such oscillations largely depends on the effective carrier mass of the specific semiconductor material.[41]

In the second panel, the dynamics up to 70 ps are shown. The bleach/SE features decay with time constants of 0.16 and 6.5 ps at 498 nm. The decay can be ascribed to the recombination of free charge carriers, and this interpretation is consistent with the disappearance of the weak oscillatory structure above 570 nm (inset). At the same time, an absorption shoulder appears around 520 nm. By 70 ps, its amplitude is larger than that of the remaining bleach. This feature might arise from lattice heating inducing a red-shift of the absorption spectrum,[22,54] superimposed by bleach/SE of remaining longer-lived electron–hole pairs which will recombine on longer timescales.

In the bottom panel the development up to 900 ps is shown. The spectra as a whole appear to experience a reduction of ΔOD values with time. The effect is possibly due to cooling of acoustic phonons (heat transfer). Two time constants are found, one of *ca.* 30 ps and another one estimated to be >1000 ps (beyond the time range of our PSCP setup) which likely describe this process.

Of particular relevance for the current study, a comparison with the PSCP data for $CH_3NH_3PbI_3$ in Fig. 3 and 5 underlines that there are no visible contributions of PbI_2 features in those transient spectra: there is no sharp bleach centered at 500 nm, and instead the broad spectral features of the perovskite in this region can be understood in terms of the bleached transition from the VB to higher-lying CBs which are located in this spectral range.[35]

4. Conclusions

Ultrafast broadband transient absorption experiments provided a comprehensive picture regarding the photoinduced dynamics of the perovskite $CH_3NH_3PbI_3$ deposited on TiO_2 scaffolds. We identified ultrafast carrier cooling processes and determined transient carrier temperatures after excitation with different excess energies above the band gap. Carrier–carrier and carrier–optical phonon scattering processes are ultrafast with time constants of <0.08, 0.2 and 2.6 ps, characterizing the transition from the coherent/non-thermal regimes to the hot-excitation regime.[38] In addition, a pronounced sub-band-gap absorption was identified for wavelengths above 750 nm on this very early timescale.

On longer timescales, the decay of acoustic phonons (τ_{AP} = 50 ps) and Auger recombination (τ_{AR} = 9, 75 and 450 ps) were clearly identified. After 700 ps, thermal equilibrium was not yet reached, with an excess carrier temperature of *ca.* 30 K. In addition, a substantial Stokes shift was found between the position of the bleach feature (band-filling) and the steady-state photoluminescence band.

Derivative-type absorption features in the transient spectra observed from energies slightly above the band gap into the UV region can be explained by a red-shift of the perovskite absorption spectrum which most likely arises from a transient Stark effect. This suggests ultrafast formation of mobile separated electrons and holes generating a substantial local electric field across the thin film. Additional contributions to the red-shift of the spectrum might also arise from lattice heating[22,44] of the perovskite, but this needs to be quantified in future experiments. Finally, in contrast to previous studies,[14] we cannot find any clear spectral signatures from lead iodide in the transient optical response of the perovskite, as shown by a comparison with the dynamics of PbI_2 on TiO_2/glass.

Acknowledgements

KO and TL thank the German Science Foundation (DFG) for financial support of this work (OU 58/10-1 and LE 926/11-1). XRD data and microscope pictures of perovskite samples were kindly provided by T. Kowald, C. Pritzel and H. F. R. Trettin (University of Siegen). We thank G. Boschloo (University of Uppsala, Sweden) for valuable discussions on perovskites and advice regarding the preparation of perovskite thin films. We also thank J. Weber and J. Schmedt auf der Günne (University of Siegen) for providing the oven for sintering the mesoporous TiO_2 layers. We are grateful to J. Troe, D. Schwarzer, K. Luther, J. Schroeder, A. M. Wodtke (Georg August University Göttingen, Germany), as well as N. P. Ernsting (Humboldt University Berlin, Germany) and J. L. Pérez Lustres (University of Santiago de Compostela, Spain) for their continuous support and advice. Finally, we would like to thank the reviewers for their valuable comments.

Notes and references

1 H. J. Snaith, *J. Phys. Chem. Lett.*, 2013, **4**, 3623.
2 N.-G. Park, *J. Phys. Chem. Lett.*, 2013, **4**, 2423.
3 S. Kazim, M. K. Nazeeruddin, M. Grätzel and S. Ahmad, *Angew. Chem., Int. Ed.*, 2014, **53**, 2812.
4 N.-G. Park, *Mater. Today*, 2015, **18**, 65.
5 H. S. Jung and N.-G. Park, *Small*, 2015, **11**, 10.

6 H.-S. Kim, C.-R. Lee, J.-H. Im, K.-B. Lee, T. Moehl, A. Marchioro, S.-J. Moon, R. Humphry-Baker, J.-H. Yum, J.-E. Moser, M. Grätzel and N.-G. Park, *Sci. Rep.*, 2012, **2**, 591.
7 M. M. Lee, J. Teuscher, T. Miyasaka, T. N. Murakami and H. J. Snaith, *Science*, 2012, **338**, 643.
8 J. M. Ball, M. M. Lee, A. Hey and H. J. Snaith, *Energy Environ. Sci.*, 2013, **6**, 1739.
9 L. Etgar, P. Gao, Z. Xue, Q. Peng, A. K. Chandiran, B. Liu, M. K. Nazeeruddin and M. Grätzel, *J. Am. Chem. Soc.*, 2012, **134**, 17396.
10 M. Liu, M. B. Johnston and H. J. Snaith, *Nature*, 2013, **501**, 395.
11 A. Marchioro, J. C. Brauer, J. Teuscher, M. Grätzel and J.-E. Moser, *Proc. SPIE*, 2013, **8811**, 881108.
12 G. Xing, N. Mathews, S. Sun, S. S. Lim, Y. M. Lam, M. Grätzel, S. Mhaisalkar and T. C. Sum, *Science*, 2013, **342**, 344.
13 S. D. Stranks, G. E. Eperon, G. Grancini, C. Menelaou, M. J. P. Alcocer, T. Leijtens, L. M. Herz, A. Petrozza and H. J. Snaith, *Science*, 2013, **342**, 341.
14 L. Wang, C. McCleese, A. Kovalsky, Y. Zhao and C. Burda, *J. Am. Chem. Soc.*, 2014, **136**, 12205.
15 F. Deschler, M. Price, S. Pathak, L. E. Klintberg, D.-D. Jarausch, R. Higler, S. Hüttner, T. Leijtens, S. D. Stranks, H. J. Snaith, M. Atatüre, R. T. Phillips and R. H. Friend, *J. Phys. Chem. Lett.*, 2014, **5**, 1421.
16 K. G. Stamplecoskie, J. S. Manser and P. V. Kamat, *Energy Environ. Sci.*, 2015, **8**, 208.
17 J. H. Heo, S. H. Im, J. H. Noh, T. N. Mandal, C.-S. Lim, J. A. Chang, Y. H. Lee, H.-j. Kim, A. Sarkar, M. K. Nazeeruddin, M. Grätzel and S. I. Seok, *Nat. Photonics*, 2013, **7**, 486.
18 J.-H. Im, C.-R. Lee, J.-W. Lee, S.-W. Park and N.-G. Park, *Nanoscale*, 2011, **3**, 4088.
19 J.-H. Im, I.-H. Jang, N. Pellet, M. Grätzel and N.-G. Park, *Nat. Nanotechnol.*, 2014, **9**, 927.
20 J. Burschka, N. Pellet, S.-J. Moon, R. Humphry-Baker, P. Gao, M. K. Nazeeruddin and M. Grätzel, *Nature*, 2013, **499**, 316.
21 F. Ehlers, M. Scholz, J. Schimpfhauser, J. Bienert, K. Oum and T. Lenzer, *Phys. Chem. Chem. Phys.*, 2015, **17**, 10478.
22 K. Oum, T. Lenzer, M. Scholz, D. Y. Jung, O. Sul, B. J. Cho, J. Lange and A. Müller, *J. Phys. Chem. C*, 2014, **118**, 6454.
23 K. Oum, P. W. Lohse, O. Flender, J. R. Klein, M. Scholz, T. Lenzer, J. Du and T. Oekermann, *Phys. Chem. Chem. Phys.*, 2012, **14**, 15429.
24 P. W. Lohse, J. Kuhnt, S. I. Druzhinin, M. Scholz, M. Ekimova, T. Oekermann, T. Lenzer and K. Oum, *Phys. Chem. Chem. Phys.*, 2011, **13**, 19632.
25 K. Golibrzuch, F. Ehlers, M. Scholz, R. Oswald, T. Lenzer, K. Oum, H. Kim and S. Koo, *Phys. Chem. Chem. Phys.*, 2011, **13**, 6340.
26 T. Lenzer, S. Schubert, F. Ehlers, P. W. Lohse, M. Scholz and K. Oum, *Arch. Biochem. Biophys.*, 2009, **483**, 213.
27 A. L. Dobryakov, S. A. Kovalenko, A. Weigel, J. L. Pérez Lustres, J. Lange, A. Müller and N. P. Ernsting, *Rev. Sci. Instrum.*, 2010, **81**, 113106.
28 B. Park, B. Philippe, T. Gustafsson, K. Sveinbjörnsson, A. Hagfeldt, E. M. J. Johansson and G. Boschloo, *Chem. Mater.*, 2014, **26**, 4466.
29 A. Cabana and C. Sandorfy, *Spectrochim. Acta*, 1962, **18**, 843.
30 N. Onoda-Yamamuro, T. Matsuo and H. Suga, *J. Phys. Chem. Solids*, 1990, **51**, 1383.
31 N. J. Jeon, J. H. Noh, Y. C. Kim, W. S. Yang, S. Ryu and S. I. Seok, *Nat. Mater.*, 2014, **13**, 897.
32 A. Grisel and P. Schmid, *Phys. Status Solidi B*, 1976, **73**, 587.
33 G. Lucovsky, R. M. White, W. Y. Liang, R. Zallen and P. Schmid, *Solid State Commun.*, 1976, **18**, 811.
34 C. Julien, H. S. Mavi and A. Chévy, *Phys. Status Solidi B*, 1993, **177**, 143.
35 A. Amat, E. Mosconi, E. Ronca, C. Quarti, P. Umari, M. K. Nazeeruddin, M. Grätzel and F. De Angelis, *Nano Lett.*, 2014, **14**, 3608.
36 P. Umari, E. Mosconi and F. De Angelis, *Sci. Rep.*, 2014, **4**, 4467.
37 K. Kash and J. Shah, *Appl. Phys. Lett.*, 1984, **45**, 401.
38 J. Shah, *Ultrafast Spectroscopy of Semiconductors and Semiconductor Nanostructures*, Springer, Berlin, 1999.
39 R. N. Zitter, *Appl. Phys. Lett.*, 1969, **14**, 73.
40 V. I. Klimov, in *Semiconductor Nanocrystals - From Basic Principles to Applications*, ed. A. L. Efros, D. J. Lockwood and L. Tsybeskov, Springer, New York, 2003, p. 73.
41 K. Oum, P. W. Lohse, J. R. Klein, O. Flender, M. Scholz, A. Hagfeldt, G. Boschloo and T. Lenzer, *Phys. Chem. Chem. Phys.*, 2013, **15**, 3906.
42 K. Oum, O. Flender, P. W. Lohse, M. Scholz, A. Hagfeldt, G. Boschloo and T. Lenzer, *Phys. Chem. Chem. Phys.*, 2014, **16**, 8019.
43 M. Fakis, P. Hrobárik, O. Yushchenko, I. Sigmundová, M. Koch, A. Rosspeintner, E. Stathatos and E. Vauthey, *J. Phys. Chem. C*, 2014, **118**, 28509.
44 K. Seibert, G. C. Cho, W. Kütt, H. Kurz, D. H. Reitze, J. I. Dadap, H. Ahn, M. C. Downer and A. M. Malvezzi, *Phys. Rev. B: Condens. Matter Mater. Phys.*, 1990, **42**, 2842.
45 C. V. Shank, R. L. Fork, R. F. Leheny and J. Shah, *Phys. Rev. Lett.*, 1979, **42**, 112.
46 U. B. Cappel, S. M. Feldt, J. Schöneboom, A. Hagfeldt and G. Boschloo, *J. Am. Chem. Soc.*, 2010, **132**, 9096.
47 P. Geiregat, A. Houtepen, Y. Justo, F. C. Grozema, D. Van Thourhout and Z. Hens, *J. Phys. Chem. C*, 2014, **118**, 22284.
48 A. Dualeh, N. Tétreault, T. Moehl, P. Gao, M. K. Nazeeruddin and M. Grätzel, *Adv. Funct. Mater.*, 2014, **24**, 3250.
49 Y. Zhao and K. Zhu, *J. Phys. Chem. C*, 2014, **118**, 9412.
50 T. Supasai, N. Rujisamphan, K. Ullrich, A. Chemseddine and T. Dittrich, *Appl. Phys. Lett.*, 2013, **103**, 183906.
51 R. Kleim and F. Raga, *J. Phys. Chem. Solids*, 1969, **30**, 2213.
52 S. Acharya, S. Chouthe, H. Graener, T. Böntgen, C. Sturm, R. Schmidt-Grund, M. Grundmann and G. Seifert, *J. Appl. Phys.*, 2014, **115**, 053508.
53 C. Bauer, G. Boschloo, E. Mukhtar and A. Hagfeldt, *Chem. Phys. Lett.*, 2004, **387**, 176.
54 A. Yamamoto, H. Nakahara, S. Yano, T. Goto and A. Kasuya, *Phys. Status Solidi B*, 2001, **224**, 301.